Published in final edited form as:
Polymer (Guildf). 2014 January 14; 55(1): 445–452. doi:10.1016/j.polymer.2013.06.019.

Fabrication of Cell Patches Using Biodegradable Scaffolds with a Hexagonal Array of Interconnected Pores (SHAIPs)

Yu Shrike Zhang[a], **Junjie Yao**[b], **Lihong V. Wang**[b], and **Younan Xia**[a,*]

[a]The Wallace H. Coulter Department of Biomedical Engineering, Georgia Institute of Technology and Emory University, Atlanta, Georgia 30332, USA

[b]Department of Biomedical Engineering, Washington University in St. Louis, St. Louis, Missouri 63130, USA

Abstract

Cell patches are widely used for healing injuries on the surfaces or interfaces of tissues such as those of epidermis and myocardium. Here we report a novel type of porous scaffolds made of poly(D,L-lactic-*co*-glycolic acid) for fabricating cell patches. The scaffolds have a single layer of spherical pores arranged in a unique hexagonal pattern and are therefore referred to as "scaffolds with a hexagonal array of interconnected pores (SHAIPs)". SHAIPs contain both uniform pores and interconnecting windows that can facilitate the exchange of biomacromolecules, ensure homogeneous cell seeding, and promote cell migration. As a proof-of-concept demonstration, we have created skeletal muscle patches with a thickness of approximately 150 μm using SHAIPs. The myoblasts seeded in the scaffolds maintained high viability and were able to differentiate into multi-nucleated myotubes. Moreover, neovasculature could efficiently develop into the patches upon subcutaneous implantation *in vivo*.

Keywords

porous scaffolds; cell patches; C2C12 myoblasts; photoacoustic microscopy; tissue engineering; regenerative medicine

1. Introduction

The field of regenerative medicine has achieved tremendous progress in recent years with a goal to restore functional tissues that are damaged by injuries or diseases. Although the tissues to be engineered are thick (over several millimeters) in many cases, the regeneration for certain injuries on the surfaces or interfaces requires the use of patch-like matrices with thicknesses on the order of sub-millimeters, such as renal epithelium, epidermis and myocardium. To realize the aim of healing these tissues from injuries, biomedical engineers have long been seeking various solutions. One promising approach conceived by Okano and co-workers is based on a technology known as the "cell sheet engineering" [1–6]. In this technology, the cells are cultured in Petri dishes coated with a layer of thermoresponsive

*Corresponding author: Younan Xia, Ph.D., The Wallace H. Coulter Department of Biomedical Engineering, Georgia Institute of Technology and Emory University, Atlanta, Georgia 30332, USA. Telephone: +1 404 385 3209; fax: +1 404 894 4243; younan.xia@bme.gatech.edu.

polymer, the poly(N-isopropylacrylamide) (pNIPAAm). Upon confluence, the cell sheets can be spontaneously detached by reducing the temperature at which pNIPAAm becomes hydrophilic and therefore inhibits cell adhesion. Due to its ease of operation, the cell sheet technology has been adopted to generate cell patches for a variety of applications including the regeneration of cornea [7], oral mucosal epithelium [3], and myocardium [8–12]. Despite these huge successes, however, there are several issues associated with the cell sheet technology. For example, the cell sheets are typically fragile and tend to crimple or fracture, which makes them inconvenient for a surgical procedure. More importantly, because the cell sheets are only composed of no more than a few layers of cells, the inadequate thickness (around 10–30 μm) would potentially hinder their use in large wounds which are much more common in humans than in small laboratory animals.

A number of alternative approaches have been developed that focus on the inclusion of three-dimensional (3D) porous scaffolds [13, 14]. Scaffolds with interconnected pores can function as physical supports for cells to attach and expand over a relatively large volume. They are therefore well-suited as matrices for the creation of thick, cellularized patches to repair large wounds. Nonetheless, the scaffolds used in most previous studies are fabricated by stochastic porogen leaching methods. As a result, these scaffolds usually exhibit completely random structures and large batch-to-batch variations, and the resulting poor interconnectivity may potentially prevent the eventual formation of homogeneous tissues [15]. To this end, the recently developed 3D porous scaffolds with an inverse opal structure have come to our attention because of their long-range well-ordered structure, uniform pores and interconnecting windows, as well as high reproducibility over different batches of fabrication [16–21]. As demonstrated in our previous publications, the high interconnectivity of these inverse opal scaffolds could facilitate the transport of biomacromolecules and migration of cells [15]. The uniform pore size and structure also made the scaffolds a well-defined system to study the effects of these parameters on cell and tissue behaviors [15, 22]. In addition, the high reproducibility associated with the production of inverse opal scaffolds is of particular importance when applying these scaffolds to clinical applications, where the generation of on-shelf products with a consistent quality is a prerequisite. To date, the inverse opal scaffolds have been extensively used in culturing immune cells and embryonic stem cells [23, 24], neovascularization [22, 25], and bone [26, 27], cartilage [28, 29], liver [30], cardiac [31], and neural tissue engineering [32], among others [33–36].

Here we report a novel category of porous scaffolds made from poly(D,L-lactic-*co*-glycolic) acid (PLGA), which is essentially an extension from the inverse opal scaffolds. Different from the inverse opal scaffolds with multiple layers of pores, we have fabricated scaffolds composed of only a single layer of pores with a unique hexagonal arrangement. We call them “scaffolds with a hexagonal array of interconnected pores (SHAIPs)”. Through the use of SHAIPs, relatively thick cell patches (a few hundred micrometers) with homogeneous tissue distribution could be fabricated thanks to the uniform pores and interconnecting windows of the scaffolds. As a proof-of-concept demonstration, we created skeletal muscle patches by seeding C2C12 murine myoblasts into SHAIPs, and then examined the differentiation of the cells and neovascularization in the patches *in vitro* and *in vivo*, respectively. When necessary, a few side-by-side comparisons were also made between the patches obtained from SHAIPs and scaffold-free myoblast sheets.

2. Materials and methods

2.1. Chemicals and materials

Gelatin (Type A, from porcine skin), sorbitan monooleate (Span® 80), and toluene were used to generate uniform gelatin microspheres. PLGA (lactide:glycolide = 75:25, M_w =

66,000–107,000) and 1,4-dioxane were used to fabricate the scaffolds. All the chemicals and materials were obtained from Sigma-Aldrich (St. Louis, MO) and used as-received unless otherwise noted.

2.2. Preparation of monolayer inverse opal scaffolds

PLGA SHAIPs were fabricated by modifying our previously published procedures for fabricating inverse opal scaffolds [15, 23, 27, 37–41]. Briefly, a methanol suspension of gelatin microspheres was slowly dropped from the elevated end of a rectangular mold made of polydimethylsiloxane (PDMS, Dow Corning, Midland, MI) positioned at a tilt angle of about 15 degrees. The mold was then gently tapped to obtain a monolayer of hexagonally packed gelatin microspheres. The mold containing the hexagonal array was sealed in a Nalgene® jar filled with methanol and placed in an oven heated at 80 °C for 1 h to induce necking between the adjacent gelatin microspheres. After cooling down to room temperature, the lattice pellet was carefully harvested by a spatula, placed on a filter paper to allow methanol to evaporate completely, and then infiltrated with a PLGA solution in 1,4-dioxane (20 wt.%). After removing the excess PLGA solution on both sides of the structure with a filter paper, the sample was frozen in a refrigerator (−20 °C) for 5 h, and lyophilized overnight in a freeze-dryer (Labconco, Kansas City, MO). The pellet with freeze-dried PLGA was immersed in ethanol for 2 min under mild vacuum to eliminate air bubbles trapped inside and then transferred into a beaker containing 900 mL water. The sample was heated at 43 °C for 3–4 h under gentle magnetic stirring to remove the gelatin lattice.

2.3 Culture of C2C12 myoblasts

C2C12 murine myoblasts were obtained from American Type Culture Collection (ATCC, Manassas, VA). The cells were maintained in a Dulbecco's modified Eagle medium (DMEM, Invitrogen, Carlsbad, CA) supplemented with 10 vol.% heat-inactivated fetal bovine serum (FBS, ATCC, Manassas, VA) and 1 vol.% penicillin-streptomycin (P/S, Invitrogen) under 37 °C and 5% CO_2. To produce cell sheets, we devised a simple method without the need of any thermal-responsive coating. Briefly, the cells were seeded in the wells of a 96-well plate at a density of 1×10^4 cells per well. Upon culture for a few days, the myoblasts in each well could gradually form an intact cell sheet, which became easily detachable from the bottom of the well simply using a pair of tweezers. For producing cell patches, cells of approximately the same number were seeded into each scaffold using a spinner flask (125 mL capacity, Corning, NY) at 65 rpm for 2 h. The cell-seeded scaffolds were then transferred into the wells of a tissue-culture non-treated 12-well plate (1 scaffold per well), and 1 mL of culture medium was added into each well. When necessary, the differentiation of myoblasts was induced by culturing the cells in DMEM supplemented with 2 vol.% horse serum (Invitrogen) and 1 vol.% P/S for 5–10 days.

2.4. Cell proliferation assay

Cell proliferation was measured by the 3-(4,5-dimethylthiazol-2-yl)-2,5-diphenyltetrazolium bromide (MTT) assays. The assay was carried out by adding 40 μL of MTT (Invitrogen) solution in phosphate buffered saline (PBS, Invitrogen, 5 mg/mL) to each well and the sample was then incubated at 37 °C for 3 h. Finally, the culture medium was withdrawn and 1 mL isopropanol was added to each well to completely dissolve the formazan crystals. Absorbance was measured at 562 nm using a spectrophotometer (Infinite 200, TECAN, Durham, NC).

2.5. Characterization of cells, immunostainning, and histology

To visualize their proliferation, the cells were stained with calcein AM (Invitrogen, 2 μM in culture medium at 37 °C for 30 min), washed with culture medium, and then observed under an Olympus microscope equipped with Capture 2.90.1 (Olympus, Center Valley, PA).

Transverse sections were obtained by fixing the samples in a 2 vol.% glutaraldehyde solution in PBS, followed by embedding in paraffin and sectioning at a thickness of 5 μm. The samples were stained with hematoxylin and eosin and bright-field transmission optical micrographs were taken using a Nanozoomer Digital Pathology (Hamamatsu, Bridgewater, NJ).

Differentiated myoblasts were fixed in a 4 vol.% formaldehyde solution in PBS. Alexa-568 phalloidin (Invitrogen) was used to stain f-actin (1:100 dilution). Myotubes were stained using mouse anti-myogenin primary antibody (Abcam, Cambridge, MA, 1:200 dilution) and Alexa-488 goat anti-mouse secondary antibody (Invitrogen, 1:200 dilution). Nuclei were counter-stained with 4′,6-diamidino-2-phenylindole (DAPI, Invitrogen). The staining results were examined using a confocal laser scanning microscope (CLSM, LSM 510, Zeiss, Thornwood, NY).

2.6. Animals and histology

All animal experiments were performed in accordance with protocols approved by the Washington University Department of Comparative Medicine and the Animal Studies Committee. Athymic Nude mice 4–5 weeks old were obtained from Harlan (Indianapolis, IN) and housed under specific pathogen-free conditions in the animal facility at Washington University in St. Louis. Scaffolds with a size of approximately 2×2 mm^2 were implanted subcutaneously into ears of the mice at one scaffold per ear per mouse [41]. At 4 weeks post-implantation, all animals were euthanized using sodium pentobarbital (200 mg/kg, IP) prior to explantation of the scaffolds. The ears of the mice were immediately collected, fixed in a 4 vol.% formaldehyde solution in PBS for 24 h and then dehydrated and embedded in paraffin wax. Serial sections (5 μm in thickness) were collected on glass slides and stained with hematoxylin and eosin. The slides were imaged using a Nanozoomer Digital Pathology slide scanner. Quantifications of both the blood vessel density and the blood vessel-to-tissue area-ratio within the scaffold areas were obtained using the ImageJ software (National Institute of Health, NIH, Bethesda, MD). Blood vessel density was determined by normalizing the number of blood vessels of a section to the area of the section, and was expressed as number per unite area (#/mm^2). Blood vessel-to-tissue area ratio was defined as the percentage (%) of total area of all the blood vessels in a tissue/scaffold section to the total area of the section.

2.7. Statistical Analysis

Quantitative data were obtained by measuring vessels from at least 5 random sections for each sample ($n = 3$). Results were reported as mean ± standard deviation.

2.8. Optical Resolution Photoacoustic microscopy (OR-PAM)

The OR-PAM system used in this study had a lateral resolution of approximately 5 μm, an axial resolution of approximately 15 μm and a penetration depth of approximately 1.2 mm in soft tissues [42, 43]. A tunable dye laser (CBR-D, Sirah, Kaarst, Germany) pumped by a Nd:YLF laser (INNOSAB, 523 nm, Edgewave, Würselen, Germany) was used as the excitation source. The short pulses (5 ns) from the dye laser were focused by a microscope objective (4×, NA = 0.1, Olympus America, Center Valley, PA) into the surface of the sample. The photoacoustic signals were detected by a spherically focused ultrasonic

transducer (V214-BC-RM, central frequency: 50 MHz, Olympus-NDT, Waltham, MA), which was placed confocally with the objective. An ultrasound/light splitter, composed of a thin layer of silicone oil sandwiched between a right-angle prism and a rhomboid prism, was used for the co-axial alignment of the optical and acoustic beams. A plano-convex lens attached onto the top of the splitter corrected the refraction of the prisms. Ultrasound gel was used as the matching medium for acoustic propagation. A motion controller provided trigger signals for laser firing, data acquisition, and raster scanning.

2.9. Scanning electron microscopy (SEM)

SEM (Nova NanoSEM 2300, FEI, Hillsboro, OR) was used to characterize the scaffolds. Prior to imaging, the samples were sputter-coated with gold for 60 s. Images were taken at an accelerating voltage of 5 kV.

3. Results and Discussion

3.1. PLGA SHAIPs and C2C12 myoblasts culture in the scaffolds

The inverse opal scaffold is a 3D porous structure fabricated by templating against a cubic close packed lattice of microspheres with uniform sizes [15, 23, 27, 37–41]. When the lattice is only comprised of a single layer of microspheres, the resulting scaffold becomes what we refer to as the SHAIP. Fig. 1A shows a schematic of the typical process for the fabrication of a SHAIP. Firstly, the uniform microspheres of gelatin are packed into a single-layer-lattice, followed by thermal annealing to induce necking between adjacent microspheres. Secondly, a solution containing the scaffolding material is infiltrated into the void space of the lattice and freeze-dried. Finally, the microspheres are selectively removed, leaving behind only the porous scaffold. It is important to note a few unique features of SHAIPs: *i*) The pore size (the size of the spherical pores) is uniform, which is inherited from the monodispersity of the microspheres used as the template (Fig. 1B). The pore size (and thus the corresponding thickness) of a scaffold is readily adjustable within a wide range of approximately 50–1000 μm depending on the size of the templating microspheres. *ii*) Each pore has six windows in uniform size connecting to adjacent pores (Fig. 1C). The size of these windows is typically about 15–20% of the pore size and can be precisely adjusted by controlling the conditions under which the gelatin microspheres are annealed [40]. The uniform pores and windows represent a unique feature of SHAIPs since they can facilitate the diffusion of nutrients and wastes, ensure the homogenous distribution of cells at the time of seeding, and promote the migration of cells during the culture [15]. *iii*) There are two openings on the two sides of each pore, which are defined as the surface pores (Fig. 1C) [25, 40]. Typically, the excess solution on both surfaces of a templating lattice is removed by wiping with a filter paper. The solution remaining in the meniscus among adjacent microspheres then solidifies after freeze-drying to form circular pores with a size slightly smaller than the diameter of the templating microspheres. These large and uniform surface pores can greatly facilitate the seeding of cells into the scaffold and potentially also induce the formation of a better tissue-scaffold interface when implanted *in vivo*. Importantly, the size of these surface pores can be finely tuned as well, depending on the properties of the solution containing the scaffolding material [40].

In this work, we fabricated PLGA SHAIPs by templating against gelatin microspheres of 200 μm in diameter. Fig. 2, A and B, shows SEM images of a single-layered gelatin lattice after thermal annealing and a PLGA scaffold, respectively, at tilt angles. The gelatin microspheres were annealed at 75–80 °C for 1 h, resulting in a window size of approximately 40 μm (20% of the pore size). We used a 20 wt.% PLGA solution in 1,4-dioxane as the infiltration solution, so that the size of the surface pores was 60–70% of the pore size, *i.e.*, the scaffolds had a surface pore size of approximately 130 μm. The ordered

arrangement of the gelatin microspheres and the uniform pore size of the scaffold could be more clearly observed in optical micrographs (Fig. 2, C and D). As shown in Fig. 2, E and F, both the monolayer gelatin lattice and the PLGA SHAIP were robust enough to be handled with a pair of tweezers. The overall flexibility of the SHAIP also potentially allows the scaffold to conform to the shape of an injury site and adhere well to that surface, thus expediting the healing process.

3.2. Proliferation of myoblasts in vitro

C2C12 mouse myoblasts were seeded into the porous scaffolds using a spinner flask and maintained in a proliferation medium. The cells were visualized using a fluorescence microscope after staining the cytoplasm with calcein AM. As shown in Fig. 3A, the cells were distributed homogeneously across the entire region of the scaffold at day 1 post-seeding and they mainly stretched along the polymer backbones. By day 7, the cells could occupy most of the void spaces of the pores (Fig. 3B).

We then quantified the proliferation of myoblasts in PLGA SHAIPs (with dimensions of 4 × 8 × 0.15 mm^3). As shown in Fig. 3C, the cells proliferated fast at the initial stage from days 1–7 to reach confluence in the scaffolds. The proliferation rates slowed down remarkably after 7 days of culture. It is further noted that, the cells in the scaffold could still maintain their viability at a reasonable level after they had reached confluence. This observation should be attributed to the relatively small thickness of these scaffolds (about 150 μm) that is close to the diffusion limits of biomolecules, unlike their thicker (>1 mm) counterparts where the cells in the bulk of the scaffolds tend to undergo apoptosis or necrosis during prolonged culture *in vitro* due to the insufficient supply of oxygen and nutrients [27].

To examine 3D cell distribution, we next obtained sections along the transverse plane of the SHAIP constructs as well as the cell sheets. Fig. 4, A and B, shows representative micrographs of hematoxylin and eosin stained sections. While the thickness of a cell sheet was largely confined to about 20–30 μm (Fig. 4A), cell patches fabricated using the SHAIP could support the distribution of cells throughout the entire thickness (about 150 μm) of the scaffold (Fig. 4B). In addition, because of the very thin structure of the cell sheet, it tended to fold significantly when released from the bottom of a culture well (Fig. 4C), which potentially renders its handling relatively inconvenient during a surgery. The cell sheet technology is also unlikely to be used for deep/large wounds that occur more commonly in large animals including humans unless stacking of multiple layers of cell sheets is performed [44]. The stacking, however, may complicate their handling in a surgical procedure. By contrast, a cellularized SHAIP was free-standing, and could be easily picked up with a pair of tweezers (Fig. 4D), thus facilitating their use in a surgery. The greater thickness of these patches based on SHAIPs is also advantageous when they are used for repairing large and deep wounds on surfaces or interfaces.

3.3. Differentiation of myoblasts in vitro

We then investigated the ability of myoblasts to differentiate in PLGA SHAIPs, since the functional recovery of skeletal muscles is highly dependent on the efficient formation of myotubes [45]. After 3 days of culture in a proliferation medium, SHAIPs populated by myoblasts were transferred into a differentiation medium for 10 additional days and then subjected to immunostaining. Fig. 5, A–D, shows a transmission optical micrograph of the cell-scaffold construct, and fluorescence micrographs of stainings for f-actin, myogenin, and nuclei of the cells, respectively. A superimposed image is indicated in Fig. 5E. It could be observed from the images that, most of the cells became myogenin-positive, confirming the differentiation of myoblasts. Interestingly, unlike the uniform distribution of cells when they were cultured in the proliferation medium (Fig. 3B), the differentiated myoblasts formed

individual cell bodies in the pores (each cell body per pore), and any of the two adjacent cell bodies were connected by elongated, aligned myotubes through the interconnecting window between the two pores. Similar organization of the cells was also described by Lin and co-workers where they induced the differentiation of myoblasts in gelatin-based inverse opal scaffolds [21], indicating that the behaviors of these cells were more dependent on the structure rather than the material of a scaffold. From an enlarged view of the superimposed image (Fig. 5F), the presence of multi-nucleated myotubes that connected the adjacent cell bodies were clearly visible.

3.4. In vivo evaluation

Skeletal muscles are highly vascularized in order to provide them with sufficient supplies of oxygen and nutrients for their strong metabolic activity [46]. We therefore examined the capability of the myoblast patches to induce neovascularization. After culturing in a differentiation medium, the patches based on SHAIPs were implanted subcutaneously in the ears of nude mice (1 scaffold per ear per mouse) [41]. The scaffolds were positioned on top of the central cartilage but below the dermis where the majority of blood vessels resided, such that the vessels could only invade into the scaffolds from the top surfaces. Neovascularization was examined non-invasively using OR-PAM at 2 weeks post implantation [41, 47, 48]. Fig. 6A, top and bottom panels, shows coronal and sagittal maximum amplitude projection (MAP) images, respectively, of neovasculature developed in a hexagonal array scaffold patch. The boundary of the patch is indicated by a white dotted square in each image. It is obvious that the neovasculature could develop uniformly throughout the entire volume of the patch thanks to the high interconnectivity of the scaffold.

The formation of muscles and blood vessels was further examined via histology at 4 weeks post implantation. Fig. 6B shows a bright-field optical micrograph of hematoxylin and eosin stained vertical sections of the implant from a SHAIP patch. Partially aligned muscle bundles with a uniform thickness encompassing a few blood vessels (indicated by yellow arrowheads) developed upon implantation, possibly originated from the aligned myotubes connecting the adjacent cell bodies in the patch. Quantitative analyses revealed that, the patches induced the formation of a blood vessel density of $86.08 \pm 13.55/mm^2$ and a blood vessel-to-tissue area ratio of $3.03 \pm 0.48\%$. Comparing with our previous study where inverse opal scaffolds with a comparable pore size were used, such ratio for the SHAIPs was remarkably larger than that in the bulk but similar to that close to the surface of the inverse opal scaffolds [25]. This result is reasonable because a SHAIP is in essence the top layer of an inverse opal scaffold. As a result, the blood vessels could easily penetrate into the pores from tissues on the top due to the large surface pore size of the SHAIP. In addition, the paracrine effect of C2C12 cells grown in the scaffold might also contribute to its high vascularity, because it is known that C2C12 cells could secret a number of angiogenic growth factors (*e.g.*, vascular endothelial growth factor) under certain stimulation [49–51].

4. Conclusion

In summary, we have successfully fabricated PLGA scaffolds consisted of a single layer of spherical pores with a hexagonal arrangement, the so-called “scaffolds with a hexagonal array of interconnected pores (SHAIPs)”. These scaffolds had a uniform pore size, high interconnectivity between the pores, as well as large openings on both surfaces. We expect that SHAIPs are likely to find widespread applications in fabricating cellularized patches for healing large wounds on surfaces or interfaces.

As a proof-of-concept demonstration, we could obtain skeletal myoblast patches with a thickness of about 150 μm by using SHAIPs. Myoblasts cultured in SHAIPs were capable of

differentiating into elongated myotubes *in vitro* and induce extensive neovascularization when implanted *in vivo*. Of course, additional work still needs to be conducted before this technique can be further extended to clinical studies. For example, although C2C12 is a well-established myoblast cell line, it does not racapitulate myogenesis as precisely as primary myoblasts [52–55]. Therefore, future investigations should include primary cultures derived directly from satellite cells. In addition, biophysical analyses (*e.g.*, force measurement) are needed to assess the functional recovery of muscles *in vivo*.

Acknowledgments

This work was supported by an NIH Director's Pioneer Award (DP1 OD000798) and startup funds from Georgia Institute of Technology (to Y.X.). This work was also sponsored by NIH grants (R01 EB000712, R01 NS46214, R01 EB008085, and U54 CA136398, to L.V.W.). Part of the research was performed at the Alafi Neuroimaging Laboratory, the Hope Center for Neurological Disorders, which is supported by the NIH Neuroscience Blueprint Center Core Grant P30 NS057105. L.V.W. has a financial interest in Microphotoacoustics, Inc. and Endra, Inc., which, however, did not support this work.

References

1. Yamato M, Okano T. Cell sheet engineering. Mater Today. 2004; 7:42–7.
2. Yang J, Yamato M, Kohno C, Nishimoto A, Sekine H, Fukai F, et al. Cell sheet engineering: recreating tissues without biodegradable scaffolds. Biomaterials. 2005; 26:6415–22. [PubMed: 16011847]
3. Yang J, Yamato M, Nishida K, Ohki T, Kanzaki M, Sekine H, et al. Cell delivery in regenerative medicine: the cell sheet engineering approach. J Control Release. 2006; 116:193–203. [PubMed: 16890320]
4. Yang J, Yamato M, Shimizu T, Sekine H, Ohashi K, Kanzaki M, et al. Reconstruction of functional tissues with cell sheet engineering. Biomaterials. 2007; 28:5033–43. [PubMed: 17761277]
5. Isenberg BC, Tsuda Y, Williams C, Shimizu T, Yamato M, Okano T, et al. A thermoresponsive, microtextured substrate for cell sheet engineering with defined structural organization. Biomaterials. 2008; 29:2565–72. [PubMed: 18377979]
6. Haraguchi Y, Shimizu T, Sasagawa T, Sekine H, Sakaguchi K, Kikuchi T, et al. Fabrication of functional three-dimensional tissues by stacking cell sheets *in vitro*. Nat Protoc. 2012; 7:850–8. [PubMed: 22481530]
7. Nishida K, Yamato M, Hayashida Y, Watanabe K, Yamamoto K, Adachi E, et al. Corneal reconstruction with tissue-engineered cell sheets composed of autologous oral mucosal epithelium. N Engl J Med. 2004; 351:1187–96. [PubMed: 15371576]
8. Shimizu T, Yamato M, Isoi Y, Akutsu T, Setomaru T, Abe K, et al. Fabrication of pulsatile cardiac tissue grafts using a novel 3-dimensional cell sheet manipulation technique and temperature-responsive cell culture surfaces. Circ Res. 2002; 90:e40–e8. [PubMed: 11861428]
9. Shimizu T, Yamato M, Kikuchi A, Okano T. Cell sheet engineering for myocardial tissue reconstruction. Biomaterials. 2003; 24:2309–16. [PubMed: 12699668]
10. Miyahara Y, Nagaya N, Kataoka M, Yanagawa B, Tanaka K, Hao H, et al. Monolayered mesenchymal stem cells repair scarred myocardium after myocardial infarction. Nat Med. 2006; 12:459–65. [PubMed: 16582917]
11. Masuda S, Shimizu T, Yamato M, Okano T. Cell sheet engineering for heart tissue repair. Adv Drug Delivery Rev. 2008; 60:277–85.
12. Shimizu T, Sekine H, Yamato M, Okano T. Cell sheet-based myocardial tissue engineering: new hope for damaged heart rescue. Curr Pharm Design. 2009; 15:2807–14.
13. Priya SG, Jungvid H, Kumar A. Skin tissue engineering for tissue repair and regeneration. Tissue Eng Part B: Rev. 2008; 14:105–18. [PubMed: 18454637]
14. Dvir T, Kedem A, Ruvinov E, Levy O, Freeman I, Landa N, et al. Prevascularization of cardiac patch on the omentum improves its therapeutic outcome. Proc Natl Acad Sci USA. 2009; 106:14990–5. [PubMed: 19706385]

15. Choi S-W, Zhang Y, Xia Y. Three-dimensional scaffolds for tissue engineering: the importance of uniformity in pore size and structure. Langmuir. 2010; 26:19001–6. [PubMed: 21090781]
16. Ma PX, Choi J-W. Biodegradable polymer scaffolds with well-defined interconnected spherical pore network. Tissue Eng. 2001; 7:23–33. [PubMed: 11224921]
17. Kotov NA, Liu Y, Wang S, Cumming C, Eghtedari M, Vargas G, et al. Inverted colloidal crystals as three-dimensional cell scaffolds. Langmuir. 2004; 20:7887–92. [PubMed: 15350047]
18. Marshall AJ, Ratner BD. Quantitative characterization of sphere-templated porous biomaterials. AIChE J. 2005; 51:1221–32.
19. Stachowiak AN, Bershteyn A, Tzatzalos E, Irvine DJ. Bioactive hydrogels with an ordered cellular structure combine interconnected macroporosity and robust mechanical properties. Adv Mater. 2005; 17:399–403.
20. Choi S-W, Xie J, Xia Y. Chitosan-based inverse opals: three-dimensional scaffolds with uniform pore structures for cell culture. Adv Mater. 2009; 21:2997–3001. [PubMed: 19710950]
21. Lin J-Y, Lin W-J, Hong W-H, Hung W-C, Nowotarski SH, Gouveia SM, et al. Morphology and organization of tissue cells in 3D microenvironment of monodisperse foam scaffolds. Soft Matter. 2011; 7:10010–6.
22. Choi S-W, Zhang Y, MacEwan MR, Xia Y. Neovascularization in biodegradable inverse opal scaffolds with uniform and precisely controlled pore sizes. Adv Healthcare Mater. 2013; 2:145–154.
23. Stachowiak AN, Irvine DJ. Inverse opal hydrogel-collagen composite scaffolds as a supportive microenvironment for immune cell migration. J Biomed Mater Res A. 2008; 85A:815–28. [PubMed: 17937415]
24. Zhang Y, Xia Y. Formation of embryoid bodies with controlled sizes and maintained pluripotency in three-dimensional inverse opal scaffolds. Adv Funct Mater. 2012; 22:121–9.
25. Bai F, Zhang J, Wang Z, Lu J, Chang J, Liu J, et al. The effect of pore size on tissue ingrowth and neovascularization in porous bioceramics of controlled architecture *in vivo*. Biomed Mater. 2011; 6:015007. [PubMed: 21206002]
26. Cuddihy MJ, Kotov NA. Poly(lactic-co-glycolic acid) Bone Scaffolds with Inverted Colloidal Crystal Geometry. Tissue Eng A. 2008; 14:1639–49.
27. Choi S-W, Zhang Y, Thomopoulos S, Xia Y. *In vitro* Mineralization by Preosteoblasts in poly(DL-lactide-*co*-glycolide) inverse opal scaffolds reinforced with hydroxyapatite nanoparticles. Langmuir. 2010; 26:12126–31. [PubMed: 20450216]
28. Kuo Y-C, Tsai Y-T. Inverted colloidal crystal scaffolds for uniform cartilage regeneration. Biomacromol. 2010; 11:731–9.
29. Kuo Y-C, Tsai Y-T. Heparin-conjugated scaffolds with pore structure of inverted colloidal crystals for cartilage regeneration. Colloid Surf B. 2011; 82:616–23.
30. Lee J, Cuddihy MJ, Cater GM, Kotov NA. Engineering liver tissue spheroids with inverted colloidal crystal scaffolds. Biomaterials. 2009; 30:4687–94. [PubMed: 19524294]
31. Madden LR, Mortisen DJ, Sussman EM, Dupras SK, Fugate JA, Cuy JL, et al. Proangiogenic scaffolds as functional templates for cardiac tissue engineering. Proc Natl Acad Sci USA. 201010.1073/pnas.1006442107
32. Kuo Y-C, Chiu K-H. Inverted colloidal crystal scaffolds with laminin-derived peptides for neuronal differentiation of bone marrow stromal cells. Biomaterials. 2011; 32:819–31. [PubMed: 20974492]
33. Irvine DJ, Stachowiak AN, Hori Y. Lymphoid tissue engineering: Invoking lymphoid tissue neogenesis in immunotherapy and models of immunity. Semin Immunol. 2008; 20:137–46. [PubMed: 18035552]
34. Lee J, Kotov NA. Notch ligand presenting acellular 3D microenvironments for *ex vivo* human hematopoietic stem-cell culture made by layer-by-layer assembly. Small. 2009; 5:1008–13. [PubMed: 19334013]
35. Lee J, Lilly GD, Doty RC, Podsiadlo P, Kotov NA. *In vitro* toxicity testing of nanoparticles in 3D cell culture. Small. 2009; 5:1213–21. [PubMed: 19263430]

36. Peyton SR, Kalcioglu ZI, Cohen JC, Runkle AP, Van Vliet KJ, Lauffenburger DA, et al. Marrow-derived stem cell motility in 3D synthetic scaffold is governed by geometry along with adhesivity and stiffness. Biotechnol Bioeng. 2011; 108:1181–93. [PubMed: 21449030]
37. Zhang Y, Cai X, Choi S-W, Kim C, Wang LV, Xia Y. Chronic label-free volumetric photoacoustic microscopy of melanoma cells in three-dimensional porous scaffolds. Biomaterials. 2010; 31:8651–8. [PubMed: 20727581]
38. Zhang Y, Cai X, Wang Y, Zhang C, Li L, Choi S-W, et al. Noninvasive photoacoustic microscopy of living cells in two and three dimensions through enhancement by a metabolite dye. Angew Chem Int Ed. 2011; 50:7359–63.
39. Zhang Y, Choi S-W, Xia Y. Modifying the pores of an inverse opal scaffold with chitosan microstructures for truly three-dimensional cell culture. Macromol Rapid Commun. 2012; 33:296–301. [PubMed: 22231861]
40. Zhang Y, Regan KP, Xia Y. Controlling the pore sizes and related properties of inverse opal scaffolds for tissue engineering applications. Macromol Rapid Commun. 2013; 34:485–91. [PubMed: 23365045]
41. Cai X, Zhang Y, Li L, Choi S-W, MacEwan MR, Yao J, et al. Investigation of neovascularization in 3D porous scaffolds *in vivo* by photoacoustic microscopy and optical coherence tomography. Tissue Eng C. 2013; 19:196–204.
42. Maslov K, Zhang HF, Hu S, Wang LV. Optical-resolution photoacoustic microscopy for in vivo imaging of single capillaries. Opt Lett. 2008; 33:929–31. [PubMed: 18451942]
43. Hu S, Maslov K, Wang LV. Second-generation optical-resolution photoacoustic microscopy with improved sensitivity and speed. Opt Lett. 2011; 36:1134–6. [PubMed: 21479007]
44. Haraguchi Y, Shimizu T, Sasagawa T, Sekine H, Sakaguchi K, Kikuchi T, et al. Fabrication of functional three-dimensional tissues by stacking cell sheets *in vitro*. Nat Protoc. 2012; 7:850–858. [PubMed: 22481530]
45. Bach AD, Beier JP, Stern-Staeter J, Horch RE. Skeletal muscle tissue engineering. J Cell Mol Med. 2004; 8:413–22. [PubMed: 15601570]
46. Levenberg S, Rouwkema J, Macdonald M, Garfein ES, Kohane DS, Darland DC, et al. Engineering vascularized skeletal muscle tissue. Nat Biotechnol. 2005; 23:879–84. [PubMed: 15965465]
47. Wang Y, Hu S, Maslov K, Zhang Y, Xia Y, Wang LV. *In vivo* integrated photoacoustic and confocal microscopy of hemoglobin oxygen saturation and oxygen partial pressure. Opt Lett. 2011; 36:1029–31. [PubMed: 21478972]
48. Yao J, Maslov KI, Zhang Y, Xia Y, Wang LV. Label-free oxygen-metabolic photoacoustic microscopy *in vivo*. J Biomed Opt. 2011; 16:076003–11. [PubMed: 21806264]
49. Kosmidou I, Xagorari A, Roussos C, Papapetropoulos A. Reactive oxygen species stimulate VEGF production from C2C12 skeletal myotubes through a PI3K/Akt pathway. Lung Physiol. 2001; 280:L585–92.
50. Ouchi N, Shibata R, Walsh K. AMP-activated protein kinase signaling stimulates VEGF expression and angiogenesis in skeletal muscle. Circ Res. 2005; 96:838–46. [PubMed: 15790954]
51. Breen E, Tang K, Olfert M, Knapp A, Wagner P. Skeletal muscle capillarity during hypoxia: VEGF and its activation. High Alt Med Biol. 2008; 9:158–66. [PubMed: 18578647]
52. Bach AD, Stem-Straeter J, Beier JP, Bannasch H, Stark GB. Engineering of muscle tissue. Clin Plast Surg. 2003; 30:589–99. [PubMed: 14621307]
53. Marzaro M, Conconi MT, Perin L, Giuliani S, Gamba P, De Coppi P, Perrino GP, Parnigotto PP, Nussdorfer GG. Autologous satellite cell seeding improves *in vivo* biocompatibility of homologous muscle acellular matrix implants. Int J Mol Med. 2002; 10:177–82. [PubMed: 12119555]
54. Blanco-Bose WE, Yao CC, Kramer RH, Blau HM. Purification of mouse primary myoblasts based on alpha 7 integrin expression. Exp Cell Res. 2001; 265:212–20. [PubMed: 11302686]
55. Bach AD, Beier JP, Stern-Staeter J, Horch RE. Skeletal muscle tissue engineering. J Cel Mol Med. 2004; 8:413–22.

- We have fabricated scaffolds with a hexagonal array of interconnected pores (SHAIPs).
- SHAIPs have a well-ordered structure, uniform pores, and high interconnectivity.
- C2C12 myoblast patches as thick as 150 μm have been produced using SHAIPs.
- SHAIPs support *in vitro* proliferation and differentiation of myoblasts.
- SHAIPs induce extensive neovascularization upon implantation *in vivo*.

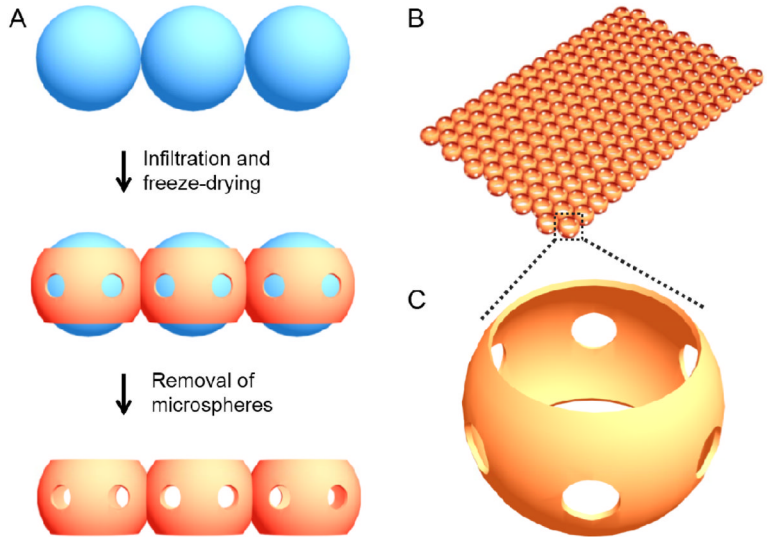

Figure 1.

A) Schematic illustration of the procedure for fabrication of a SHAIP (side view): *i*) uniform microparticles are assembled into a close-packed monolayer lattice; *ii*) the scaffolding material is infiltrated into the voids and the extra solution on both surfaces is removed with a filter paper followed by freeze-drying; *iii*) the lattice is selectively removed, leaving behind the scaffold. B) Schematic of the SHAIP, and C) an enlarged view of a pore indicating the high interconnectivity (six uniform windows connecting adjacent pores) of the scaffold.

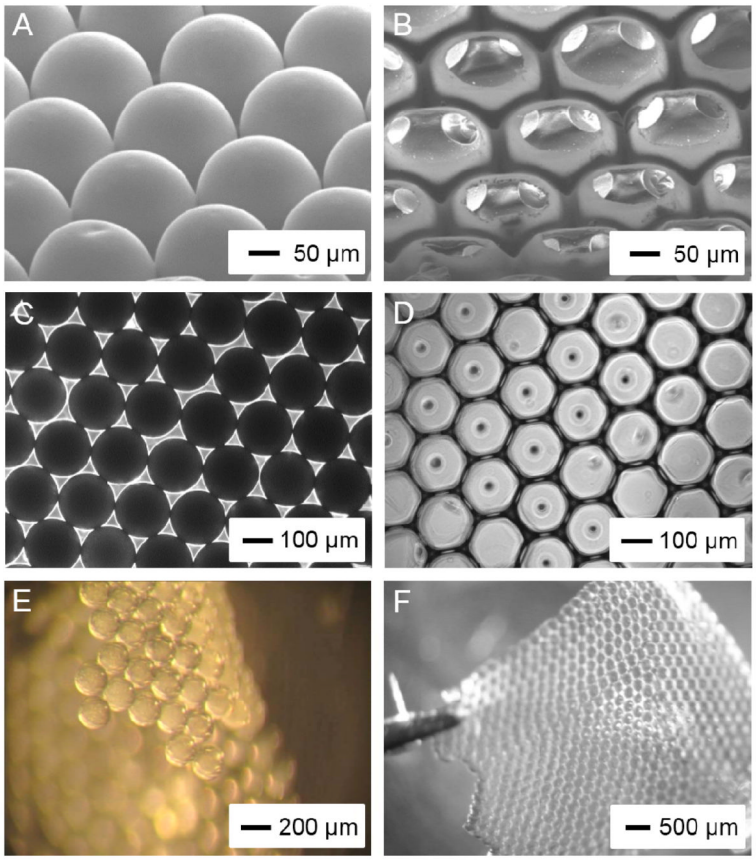

Figure 2.

A, B) SEM images showing (A) a monolayer of gelatin microspheres after thermal fusion and (B) a PLGA SHAIP after removal of the gelatin lattice, both at tilt angles. C, D) Transmission bright-field optical micrographs showing the top view of (C) a lattice of the gelatin microspheres and (D) a PLGA SHAIP. E, F) Reflection bright-field optical micrographs showing (E) a free-standing lattice of the gelatin microspheres after thermal fusion and (F) a free-standing PLGA SHAIP held by a pair of tweezers.

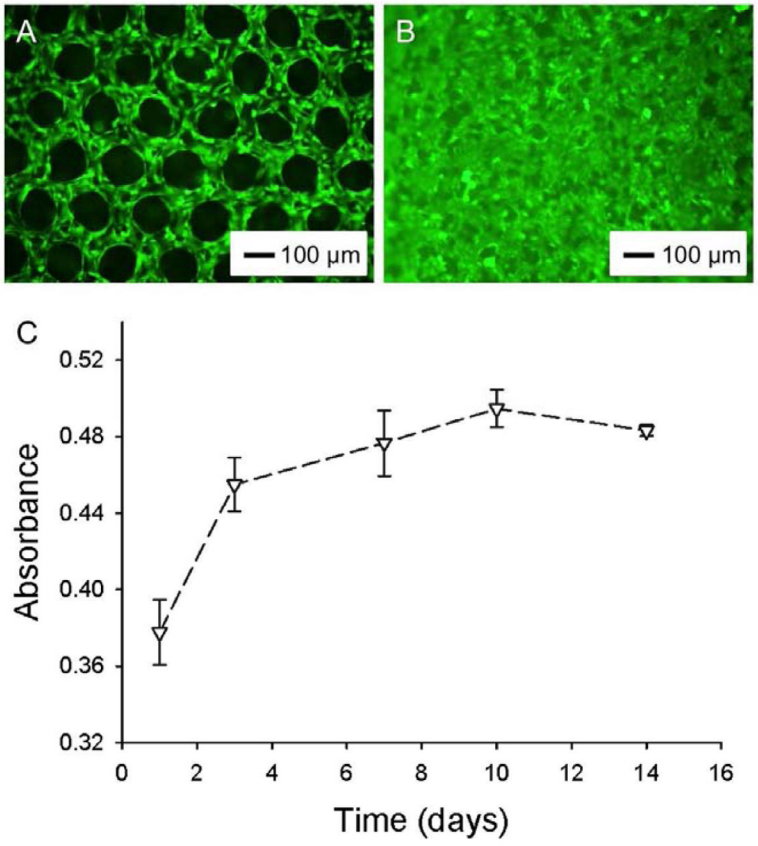

Figure 3.

A, B) Fluorescence micrographs showing C2C12 myoblasts grown in PLGA SHAIPs at days 1 and 7, respectively. The cells were stained with calcein AM for cytoplasm. C) Proliferation profile of C2C12 myoblasts cultured in PLGA SHAIPs, as determined by the MTT assay.

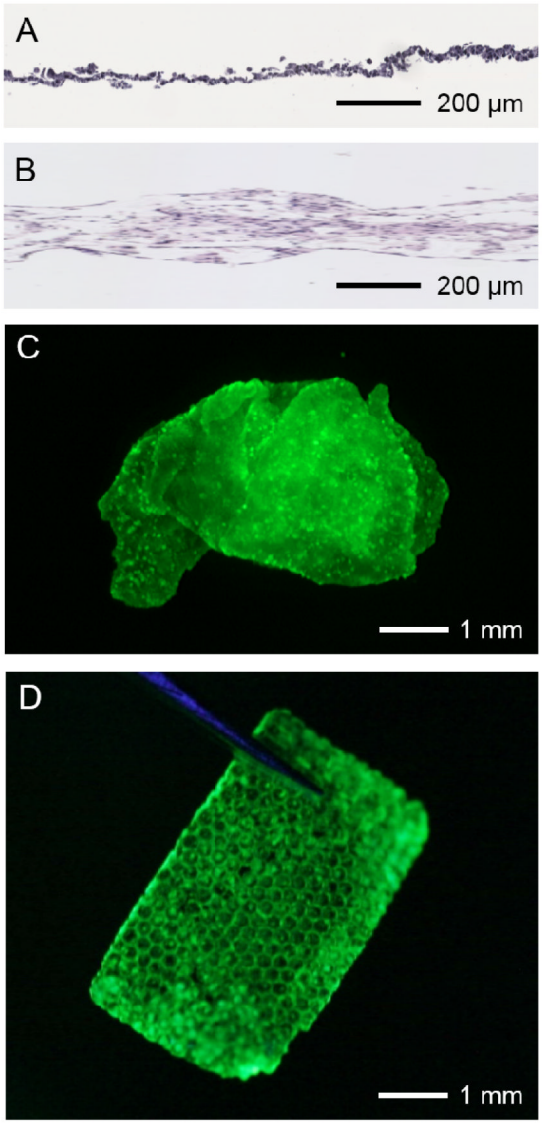

Figure 4.

A, B) Transmission bright-field optical micrographs showing hematoxylin and eosin stained transverse sections of (A) a myoblast cell sheet and (B) myoblasts grown in a PLGA SHAIP. C, D) Fluorescence micrographs showing (C) a detached myoblast cell sheet and (D) a free-standing myoblast patch in a PLGA SHAIP; the cells were stained with calcein AM for cytoplasm.

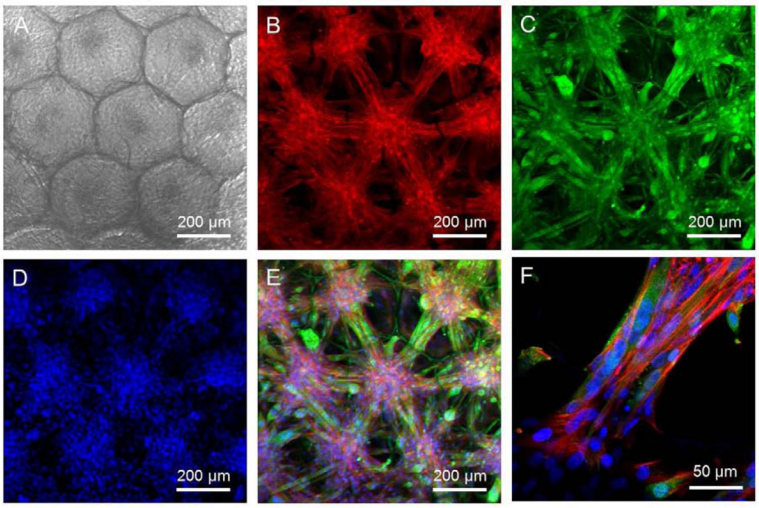

Figure 5.
C2C12 myoblasts cultured in a PLGA SHAIP in a differentiation medium for 10 days. A) A transmission bright-field optical micrograph showing the cells grown in the scaffold. B–D) CLSM images showing (B) f-actin, (C) myogenin, which is a marker for differentiated myoblasts, and (D) nuclei. E) Superimposed image of (B–D). F) An enlarged view of the superimposed image showing multinucleated myotubes connecting the cell bodies in adjacent pores.

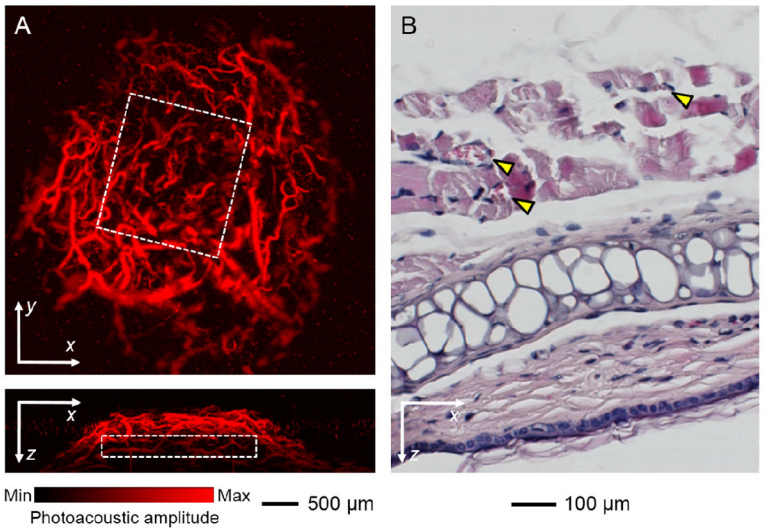

Figure 6.

A) Top panel: a coronal PAM MAP image at the depth of the implant (optical section thickness: approximately 200 μm) showing neovascularization within a myoblast patch based on PLGA SHAIP at 2 weeks post implantation; Bottom panel: corresponding sagittal PAM MAP image from the central region of the patch (optical section thickness: approximately 500 μm). The white dotted square in each image denotes the rough boundary of the patch. MAP stands for "Maximum Amplitude Projection". B) A bright-field optical micrograph showing hematoxylin and eosin stained transverse section of the implant at 4 weeks post implantation. Yellow arrowheads indicate blood vessels.